



Design of a fully integrated sensor system of a plain bearing

Janek Paeßens¹ · Karl-Heinz Kratz¹ · Tobias Gemmeke¹ · Kevin Kauth¹ · Thao Baszenski² · Benjamin Lehmann² · Georg Jacobs²

Received: 13 November 2023 / Accepted: 25 April 2024
© The Author(s) 2024

Abstract

Recent years revealed a notable trend for rolling bearings to be increasingly replaced by plain bearings for particular applications. A prominent example is the planetary stage in wind turbine gearboxes. The advantages of plain bearings are higher realizable power density due to smaller installation space compared to rolling bearings as well as the possibility of wear-free operation under ideal operational conditions. In real applications, however, plain bearings are subject to wear, for example due to start-stop processes, which lead to mixed friction conditions. Since the wear of plain bearings strongly depends on the operational conditions, monitoring is essential to detect inadmissible operating conditions. To avoid extra installation space and to achieve a minimal influence on the surrounding system, this work aims to integrate an energy-autarkic sensor system into the bearing volume to monitor the operational status of the plain bearing. To achieve autarky, the resulting data must be transmitted wirelessly and the external power supply must be eliminated. In this work, the software and hardware architecture of a sensor-integrating plain bearing prototype for monitoring the minimum oil gap height and the displacement angle of the shaft based on in-situ temperature measurements is presented. Furthermore, energy harvesting and energy saving measures are implemented and evaluated which intend to enable completely autarkic operation of the sensor integrating machine element in the future. A prototype of the sensor system is in turn used in-the-field to investigate required sampling rates and the spatial resolution of the temperature measurements.

✉ Janek Paeßens
paessens@ids.rwth-aachen.de
Karl-Heinz Kratz
kratz@ids.rwth-aachen.de
Tobias Gemmeke
gemmeke@ids.rwth-aachen.de
Kevin Kauth
kauth@ids.rwth-aachen.de
Thao Baszenski
thao.baszenski@imse.rwth-aachen.de

Benjamin Lehmann
benjamin.lehmann@imse.rwth-aachen.de
Georg Jacobs
georg.jacobs@imse.rwth-aachen.de

- ¹ Lehrstuhl für Integrierte Digitale Systeme und Schaltungsentwurf (IDS), RWTH Aachen, Aachen, Germany
- ² Lehrstuhl und Institut für Maschinenelemente und Systementwicklung (IMSE), RWTH Aachen, Aachen, Germany

Design eines vollintegrierten Sensorsystems für Gleitlager

Zusammenfassung

In den letzten Jahren ist bei bestimmten Anwendungen eine deutliche Verschiebung von Wälzlagern hin zu Gleitlagern zu beobachten. Ein prominentes Beispiel ist die Planetenstufe in Getrieben von Windkraftanlagen. Die Vorteile von Gleitlagern sind die höhere realisierbare Leistungsdichte aufgrund der geringeren Bauraumgröße im Vergleich zu Wälzlagern sowie die Möglichkeit des verschleißfreien Betriebs unter idealen Betriebsbedingungen. In realen Anwendungen unterliegen Gleitlager jedoch einem Verschleiß, beispielsweise durch Start-Stopp-Vorgänge, die zu Mischreibungszuständen führen. Da der Verschleiß von Gleitlagern stark von den Betriebsbedingungen abhängt, ist eine Überwachung unerlässlich, um unzulässige Betriebszustände zu erkennen. Um zusätzlichen Bauraum zu vermeiden und eine minimale Beeinflussung des umgebenden Systems zu erreichen, zielt diese Arbeit darauf ab, ein energieautarkes Sensorsystem zur Überwachung des Betriebszustandes des Gleitlagers in das Lagervolumen zu integrieren. Um Autarkie zu erreichen, müssen die anfallenden Daten drahtlos übertragen werden und die externe Energieversorgung muss entfallen. In dieser Arbeit wird die Hard- und Softwarearchitektur eines Prototypen für ein vollintegriertes Sensorsystem zur Überwachung der minimalen Schmierstalthöhe und des Verlagerungswinkels der Welle im Gleitlager auf Basis von in-situ Temperaturmessungen vorgestellt. Darüber hinaus werden Energy-Harvesting- und Energiesparmaßnahmen implementiert und evaluiert, die in Zukunft einen vollständig autarken Betrieb des sensorintegrierenden Maschinenelements ermöglichen sollen. Ein Prototyp des Sensorsystems wird im praktischen Einsatz getestet, um die erforderlichen Abstraten und die räumliche Auflösung der Temperaturmessung zu untersuchen.

1 Introduction

The integration of sensors into machine elements is paramount in modern engineering and manufacturing for a multitude of compelling reasons. First and foremost, it enables real-time condition monitoring. The sensors can measure critical parameters such as temperature, pressure, vibration, and more, providing valuable insights into the health and efficiency of the machine element. By continuously tracking these variables, potential issues or anomalies can be detected early, even before they become critical problems and maintenance intervals can be maximized. This early warning system is crucial for preventing unexpected breakdowns, which can result in costly downtime and repairs [1]. This holds particular significance within the context of plain bearings as they are responsible for a significant amount of failures in electrical machines [2]. Considering the abundance of applications for plain bearings, such as wind turbines, combustion engines, industrial manufacturing [3, 4] and many more, this further underlines the importance of sensor integration into plain bearings. Moreover, sensor integration harmonizes with the overarching framework of the Internet of Things (IoT) and Industry 4.0 [5, 6]. These paradigms advocate seamless interconnectivity between devices and data-driven decision-making, potentially leading to enhancements in the development, maintenance, and application process of machine elements.

A cost-effective method for monitoring plain bearings is the utilization of temperature profiles. A persistent occurrence of mixed and solid-state friction induces a sudden temperature increase in the load zone close to the running

surface [7]. Thus, mixed and solid-state friction can be detected by temperature sensors. Furthermore, DIN-Standard 31652 even provides a way to approximate the minimum oil gap height from the system shaft misalignment, given by the temperature distribution, using the Gumbel-curve [8–11].

However, in particular within the context of multi-axis rotating systems, external wiring of the sensors is often not possible. This results in the need for an energy-autarkic system. Thermogenerators (TEG) are optimally suited for energy harvesting from plain bearings due to their ability to efficiently convert the naturally occurring temperature differentials even at low-temperature differences of a few Kelvin using the Seebeck effect [12, 13]. By this, the need for an external power supply could even be omitted for some applications [14]. Besides the need for an internal power supply, the wireless system also necessitates the substitution of the wired data exchange. Resultantly, a sensor system fulfilling these demands can be declared as a Sensor-Integrated Machine Element as classified in [15].

The development of such a sensor integrating system is driven in particular by the recently rapidly advancing possibilities in the field of energy efficiency and reliability of energy harvesters [16–20] on the one hand and wireless data transmission technologies [21] on the other hand. Hence, there are not many comparable approaches for energy-autarkic sensor integrating plain bearings yet. However, the research in the field of sensor integrating machine elements including plain bearings is growing [22–24].

In Chap. 2 the chosen method to derive the minimal oil gap height from temperature sensor data using the Gumbel-curve is described and results of an experimental prototype

and corresponding conclusions are presented. In Chap. 3, a precise analysis of the energy consumption of the components of the presented sensor integrating system will be given and compared to the amount of harvestable energy. Additionally, an evaluation of different wireless data transmission technologies will be given and a conclusion regarding the possibilities of the implementation into the plain bearing will be drawn. Finally, in Chap. 4 the software architecture is described, and specific energy-saving measures are discussed.

2 Method and test setup

Basis of the approximation of the minimal oil gap height is the measurement of the temperature profile to determine the angle of the maximal temperature. This angle is associated with the minimum oil gap height by the Gumbel-curve. In the following this connection is explained in detail and corresponding results of the presented prototype are depicted. Subsequently, measures to enhance the result accuracy are discussed.

2.1 Determination of the minimum oil gap height

In hydrodynamic plain bearings, the required pressure to separate the shaft and bearing shell surfaces is generated by a lubricant film building up due to the convergent gap geometry caused by the relative motion. DIN standard 31652 represents a dimensioning guideline for the safe operation of hydrodynamic radial plain bearings [9–11]. In the DIN standard, the Reynolds equation [25] is solved for discrete operating points and provided in tabular and graphical form for the determination of the variable of interest. DIN standard 31652-2 includes the Gumbel-curve, which provides a relationship between the shaft misalignment angle β and the eccentricity ϵ . Fig. 1 displays the Gumbel-curve and the minimum oil gap height h_{min} , which was determined via the eccentricity ϵ for the bearing geometry investigated, as a function of the bearing angle φ ($\varphi = \beta + 180^\circ$).

In simulative investigations of a thermoelastohydrodynamic (TEHD) bearing model, it was shown that the bearing angle of the shaft misalignment has a high agreement with the angle of the maximum occurring temperature $\varphi_{T,max}$ on the bearing running surface [26]. The sensor system, therefore, follows the approach of measuring the relevant temperature field. The bearing angle of the maximum occurring temperature $\varphi_{T,max}$ is in turn used to determine the minimum oil gap height h_{min} via the relationship of the Gumbel-curve.

Followingly initial experimental results of a fully integrated sensor system prototype for a plain bearing are presented. The detailed concept of the system design is discussed in [27]. The prototype of the fully integrated sensor system is equipped with all electronic components necessary for data generation, processing, and energy generation incorporated into the plain bearing volume. The experimental investigations are carried out on a test rig for hydrodynamic plain bearings, which is shown schematically in Fig. 2. A detailed description of the test bench setup can be obtained from [28].

During the test, the prototype is positioned in a bearing support. The test radial force F_r is applied to the plain bearing via the bearing support (Fig. 2 center). The plain bearing is made of the bronze alloy CuSn12Ni2-C [29] and has an inner diameter of $D = 120\text{ mm}$. Further data regarding the test bearing geometry can be obtained from Fig. 1. The rotary shaft movement is realized via an electric motor. In the testing setup, a mineral oil of class ISO VG 320 is selected.

In Fig. 3 the initial prototype of the sensor system tested is shown. On the left-hand side, the rear view of the prototype, including the printed circuit board (PCB) with temperature sensors as well as the energy conversion components, is shown. On the right-hand side, the front view of the prototype including a thermogenerator for thermoelectrical energy harvesting, is displayed.

In TEHD simulations, it was shown that in the investigated tribological system edge bearing occurs [8]. The temperature field relevant for measuring shaft displacement occurs in the direct vicinity of the end faces of the bearing.

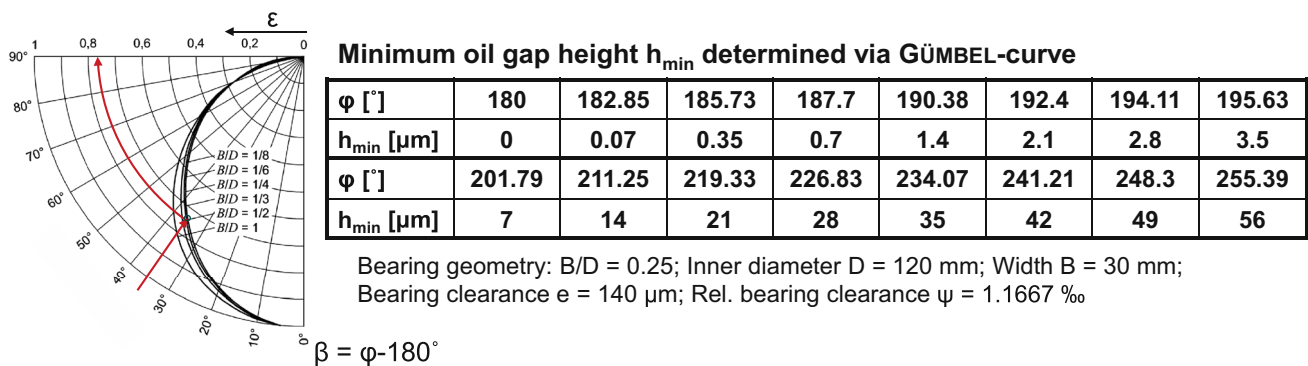


Fig. 1 Minimum oil gap heights determined via the Gumbel-curve for the examined plain bearing geometry

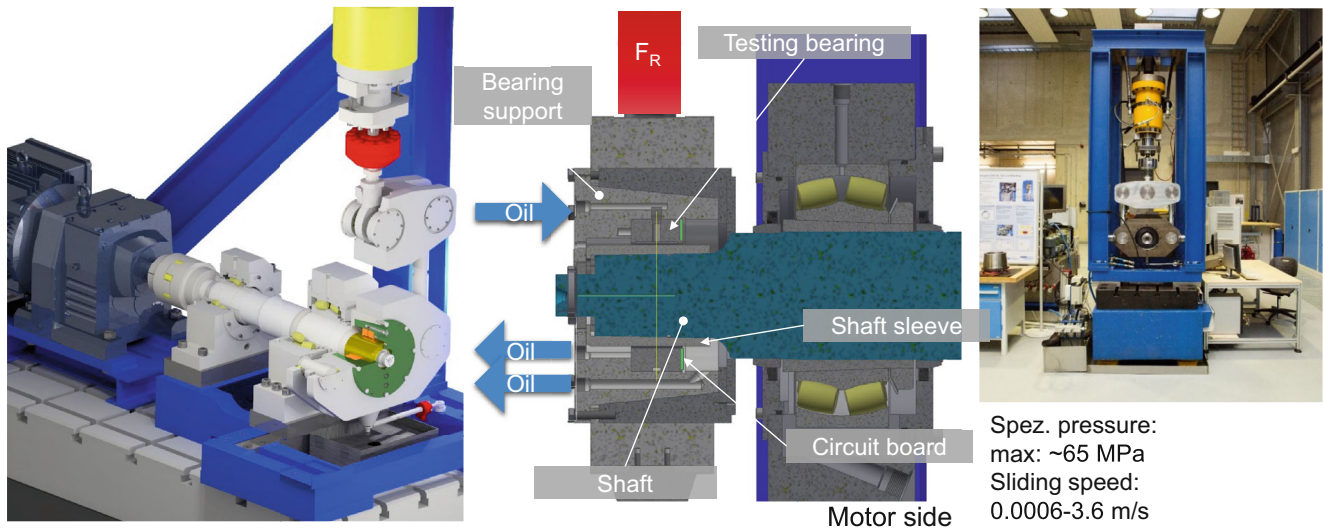
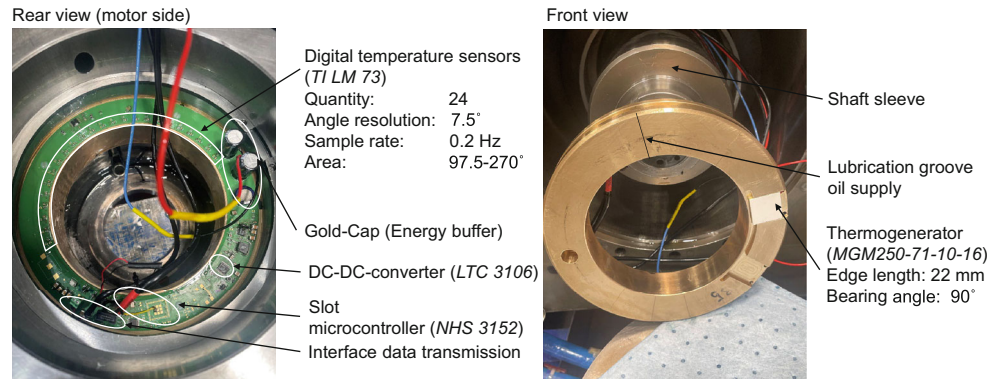


Fig. 2 Test bench setup for the experimental investigation of the condition monitoring system

Fig. 3 Prototype of an energy-autarkic, temperature-based condition monitoring system for plain bearings



Accordingly, the printed circuit board is placed in a face milling with a depth of 1 mm. The temperature sensors have thermal contact with the bearing inside the milling. The radial distance of the sensors to the running surface of the bearing is 1 mm. The temperature is measured slightly below the running surface, as measuring in the lubrication gap entails challenges. On the one hand, temperature sensors that measure in the lubrication gap could influence the lubricant film formation. On the other hand, sensors in the lubrication gap can be irreversibly damaged if mixed friction and high thermal loads occur.

The shaft of the test rig performs a rotary motion in a mathematical positive direction from the front view of the test bench (see Fig. 4 right-hand side). Therefore, the displacement of the shaft occurs within the bearing angle range of $\varphi = 180\text{--}270^\circ$ and the relevant temperature field for the temperature-based gap height determination via Gumbel-curve is localized here. However, in the first prototype of the sensor system investigated, almost the entire lower half of the bearing was equipped with temperature sensors in the range $\varphi = 97.5\text{--}270^\circ$ to be able to record the tempera-

ture distribution in a broad range. To measure temperature distribution 24 temperature sensors with an angular separation $\Delta\varphi = 7.5^\circ$ are placed on the PCB (Fig. 4 right-hand side).

2.2 Experimental results

The results of a representative test procedure for the prototype are presented below. Fig. 4 shows the test plan of the test performed at the top. A constant specific pressure of $\bar{p} = 1.388\text{ MPa}$ was used for the test. Starting from a sliding speed $\bar{v} = 3\text{ m/s}$, the sliding speed step of $\Delta\bar{v} = 0.5\text{ m/s}$ was decreased every $\Delta t = 10\text{ min}$. After $t = 60\text{ min}$ and a final sliding speed step $\bar{v} = 0.5\text{ m/s}$, the test was terminated as scheduled. The associated Sommerfeld-number ($So < 1$) is consistently in the fast-running range during the test procedure. In the center graph of Fig. 4, the measured temperature curves of the 24 temperature sensors are shown as a function of the respective angular positions over the test time.

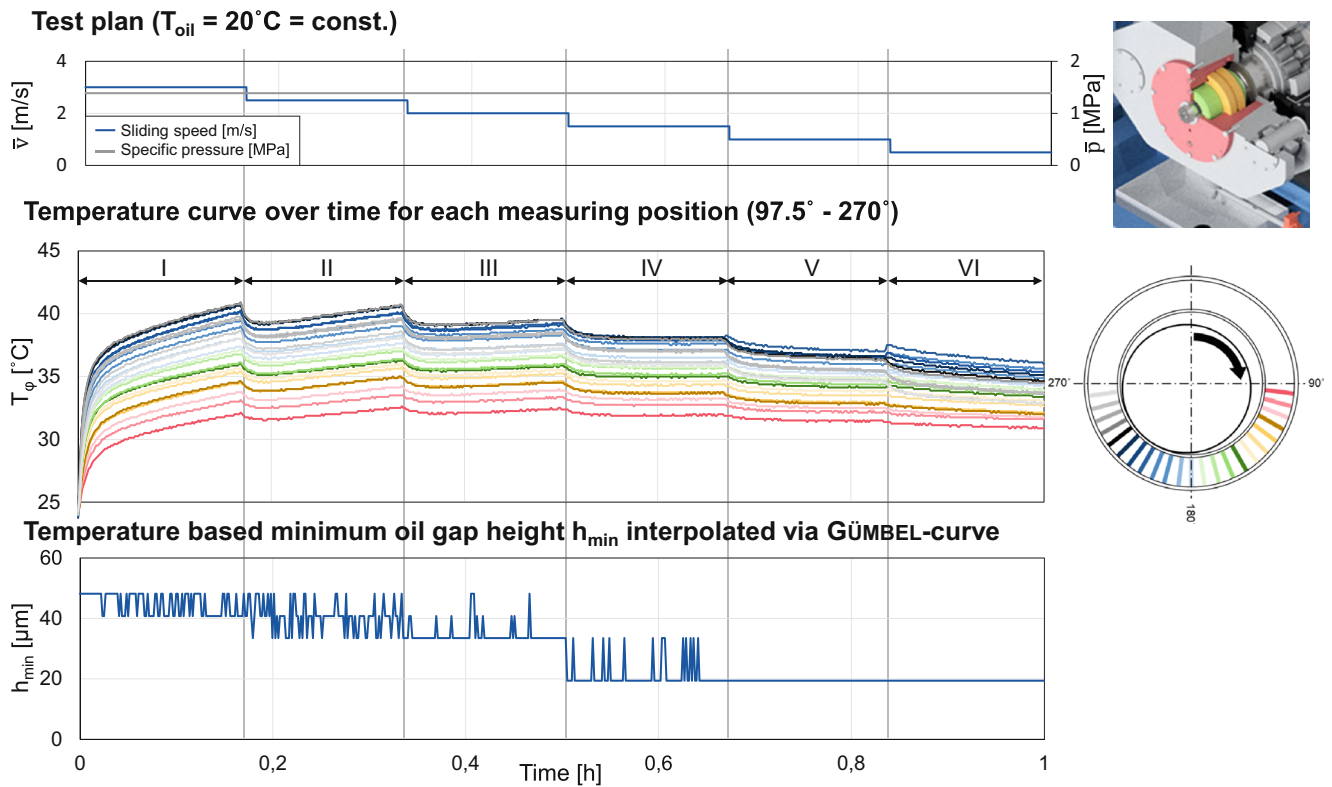


Fig. 4 Experimentally measured temperature curves and resulting oil gap heights for different sliding speeds

At the beginning of the test, the measured temperatures increased rapidly in all measuring positions. Subsequently, the temperature curves within the first-speed stage follow a degressive positive gradient. At the end of the first stage (I), the globally recorded maximum temperature of $T_{max, total} = 40.875\text{ °C}$ is reached. At this point, the difference between the minimum and maximum temperatures is $\Delta T_{t=10\text{ min}} = 8.75\text{ °C}$. The reduction of the sliding speed at the beginning of each stage is accompanied by a decline in all measuring temperatures. Subsequently, there is another degressive increase in temperatures within each speed stage. Over time, the global temperature difference ΔT_t between the maximum and minimum measured temperatures is successively decreased. The measured data are subsequently used to calculate the gap height h_{min} using the temperature-based Gumbel-curve. The angular position of the maximum temperature is determined from the test data for the respective time period. The angular position is then used to calculate h_{min} by linear interpolation using the table values shown in Fig. 1. The resulting oil gap height curve during the test is displayed in Fig. 4 below. The determined oil gap height is in the range $h_{min} = 19.41\text{--}48.21\text{ }\mu\text{m}$. It is evident that a lower sliding speed \bar{v} ($\bar{p} = 1.388\text{ MPa} = \text{const.}$) results in a lower bearing angle of the maximum temperature $\varphi_{T, max}$ and thus a lower determined h_{min} .

Examining the gap height plot, the gap height resolution is in the range of $\Delta h_{min} = 6.88\text{--}7.41\text{ }\mu\text{m}$. In this regard, it should be mentioned that the relationship between $\Delta\varphi$ and Δh_{min} depicted by the Gumbel-curve is not linear (see Fig. 1). A higher level of input value φ in the Gumbel-curve results in a higher Δh_{min} , corresponding with $\Delta\varphi$ (= const.)-value. By recording the temperatures in the lower half of the bearing, it could be shown that the relevant temperature field is always in the range $\varphi = 180\text{--}270\text{ °}$ due to the rotational direction. In the next prototype iteration, therefore, only the third quadrant will be equipped with temperature sensors. Moreover, it is possible to halve the angular resolution to $\Delta\varphi = 3.75\text{ °}$ without the sensors contacting. Accordingly, 25 temperature sensors will be placed in this quadrant in the next prototype iteration.

However, as a higher number of temperature sensors inevitably results in increased energy consumption, it is still advisable to strive for the minimization of sensor quantity in the final sensor system. To achieve this, a regression analysis of the sensor temperatures is conducted. An example of such an interpolation with a fourth-degree polynomial for randomly selected time points from previous experiments is illustrated in Fig. 5. It appears that this interpolation can potentially compensate for measurement inaccuracies and significantly enhance the angular resolution of the angle associated with the maximum temperature. However, whether

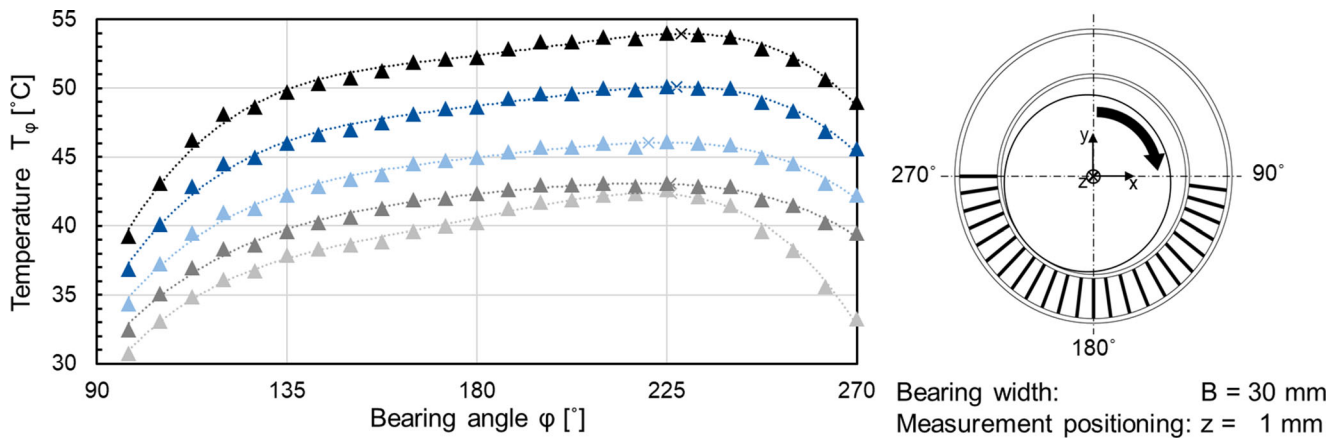


Fig. 5 Interpolation of temperature distribution at randomly sampled time points taken from previous experiments

this method provides an accurate approximation of the actual temperature distribution or if a higher angular resolution of the measurement data is necessary for a meaningful interpolation must be further assessed. This will be accomplished through the higher angular resolution of the next prototype by sampling, for instance, every second temperature sensor. An experimental validation of the temperature-based gap height determination will be performed by using inductive eddy current sensors. Two eddy current sensors are mounted flush with the surface of the plain bearing, offset by 90 degrees, to determine the kinetic shaft path [7]. The recorded shaft path in turn allows the determination of the misalignment angle β and the minimum lubrication gap height h_{min} . Additionally, an evaluation using a TEHD model is possible.

3 Energy management

In this chapter, the demand of the different components in multiple scenarios will be discussed and subsequently compared to the harvestable energy. Some simple considerations regarding this have already been made in [26]. However, the following section will update these considerations and refine them.

The energy demand of the sensor system is mainly driven by the microcontroller, the sensory and the wireless communication. Thus, energy consumption will be discussed in this outline. Other components, such as the I2C switch, will be neglected as they have comparatively low energy consumption [30].

3.1 Microcontroller

The NHS3152 supports external voltages between 1.72 and 3.6 V. According to [31], very low energy consumption can be achieved at a system clock frequency of 0.5 MHz and

an operating voltage of 1.8 V. However, 0.5 MHz clock frequency is not sufficient to operate the I2C bus at the standard mode [32] and the deep power down mode will not be used for this purpose, as this would require saving all temperature and operating information in the EEPROM resulting in additional power consumption due to write costs of $300 \mu\text{A}/\text{MHz}$ and significantly limited endurance [33]. Instead, the deep sleep mode will be used. Resultantly, the power consumption will be analyzed for the specific parameters chosen for the sensor system setup in the following. Besides, a comparison between a supply voltage of 1.8 and 3.3 V will be given.

The results of the power measurements of the microcontroller at 1.8 and 3.3 V can be found in Fig. 6. The measurements depict the power consumption of the NHS3152 during the execution of basic continuous I2C operations or during the deep sleep mode respectively. The values have been measured using a multimeter and do not cover potential short-time peaks but only averaged values. As the test

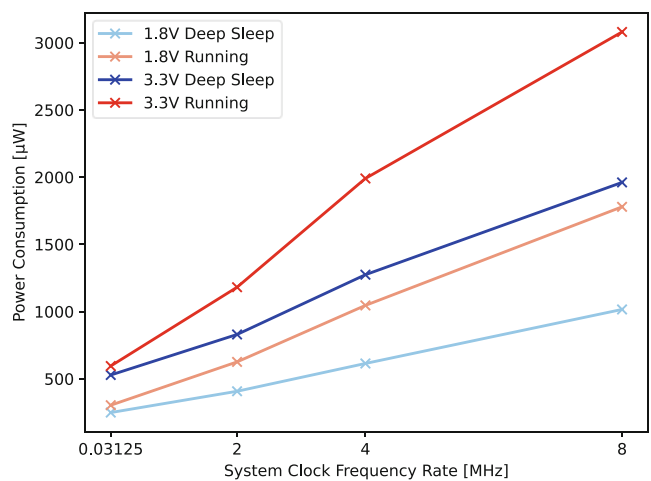


Fig. 6 Comparison of energy consumption at different system clock frequencies and supply voltages during deep sleep and active phase

setup used for these measurements differs from the actual setup of the prototype, the data should not be regarded to determine an energy budget, but only for qualitative comparison of the influence of supply voltage and system clock frequency on the energy consumption. The data reveals that energy consumption can be significantly reduced at a voltage of 1.8 V compared to a voltage of 3.3 V. Furthermore, it is apparent that the current scales with the system clock frequency. Although the system clock frequency of 31.25 kHz, that was used for the current prototype setup, results in the lowest energy consumption, it could be increased to at least 2 MHz in the next iteration to fulfill the aforementioned requirements. Additionally, this increase of the system clock frequency enables significantly shorter running periods. Therefore, despite the higher clock rate, the energy consumption of the prototype can be further reduced in the next iteration due to the transition to a supply voltage of 1.8 V and shorter active periods.

To compare the energy consumption of individual prototype components, the CPU's energy consumption was measured individually afterward. For the prototype, using a supply voltage of 3.3 V and a clock frequency of 31.25 kHz, a current of 0.298 mA in deep sleep mode and 0.457 mA during active phase was measured. Even though the combination of 3.3 V supply voltage and 31.25 kHz clock frequency may not be optimally energy-efficient, this configuration will be employed to assess the energy budget, as it corresponds to the current prototype setup.

3.2 Temperature sensors

The typical energy consumption of the LM73 temperature sensor at 3.3 V is 320 μ A during operation and 1.9 μ A during shutdown [34]. Considering 24 sensors, this results in a shutdown current of 45.6 μ A and an energy demand of 7.68 mA when operating all sensors at once. However, this power demand can be distributed temporally to avoid excessive energy peaks.

To reduce the energy requirement of the system, the voltage will be reduced to 1.8 V in future. As the LM73 does not meet this requirement, it needs to be replaced by the TMP117. In addition to a lower energy requirement, the latter also offers a higher resolution, smaller dimensions and an EEPROM for buffering measured values [35].

3.3 Wireless communication

While the wireless communication serves the main purpose of transmitting an alarm signal and does not require continuous operation, it is imperative to account for the notably substantial power consumption of the wireless components. This consideration is essential to ensure that the ESP32-C3 can operate for a sufficient duration, allowing for the trans-

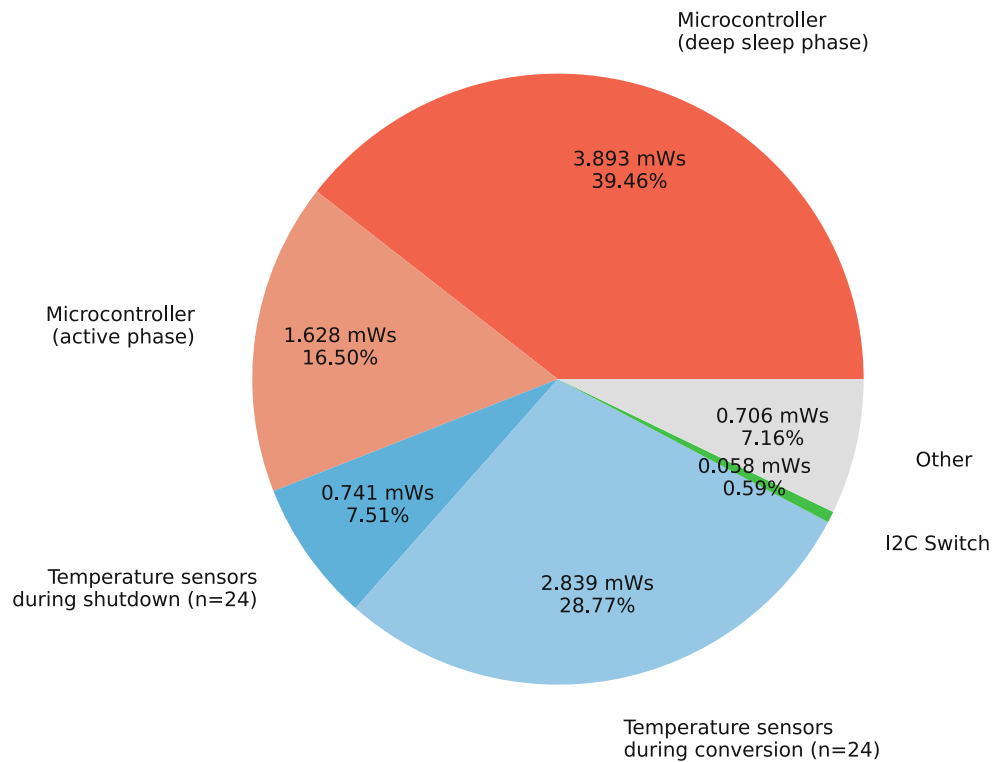
mission of the intended signal. Consequently, the impact on the energy consumption of distinct wireless protocols will be assessed and compared to the amount of energy that can be saved. The hardware configuration facilitates communication through Wi-Fi and BLE, both utilizing the ESP32-C3 module and NFC, provided by the NHS3152. However, due to the limited range of NFC and the poor accessibility of the microcontroller within the plain bearing, NFC may not be suitable for every application case. However, for NFC-compatible cases, energy consumption does not need to be considered, as the energy can be consumed from the corresponding counterpart. Thus, NFC is excluded from the scope of the discussion regarding energy consumption.

Wi-Fi and BLE present contrasting characteristics. Wi-Fi is renowned for its high data transfer rates, while BLE, in contrast, exhibits lower transfer rates, making it particularly suitable for handling small data packages. Simultaneously, BLE is engineered for exceptional energy efficiency, whereas Wi-Fi necessitates higher energy consumption. Thus, Wi-Fi is optimally suited during the development phase, as energy constraints are of minimal concern and the high data rates are advantageous for monitoring the system continuously. When transitioning to in-the-field applications, energy consumption becomes a paramount consideration, necessitating the careful selection of a wireless protocol. In this operational phase, the need for transferring substantial data volumes is generally insignificant. Thus, the priority shifts towards energy-efficient communication, as low power consumption is pivotal in ensuring prolonged device operation, making BLE optimally suited for this purpose. This conclusion is also reflected in a multitude of IoT devices [36].

3.4 Energetic feasibility conclusion

The consideration of the energy measurements of the entire system and the microcontroller, as well as the technical data of the other components results in the energy distribution depicted in Fig. 7. The given energy consumption is based on the average of a full cycle comprising an active phase of slightly more than a second and a four second deep sleep phase. The predominant share of power consumption is due to the microcontroller. The primary reason for this is that the NHS3152 exhibits only a low reduction in power consumption during the deep sleep phase. Furthermore, the power consumption of the temperature sensors also constitutes a significant portion of the overall energy consumption. Notably, this energy consumption is concentrated almost exclusively during the active phase. The measured energy consumption not covered by these considerations is caused by other small energy consumers, such as pull up resistors and capacitors.

Fig. 7 Energy consumption breakdown of the presented system of a full cycle



The above considerations result in an average power of $\bar{P} = \frac{9.866 \text{ mWs}}{5.0388 \text{ s}} = 1.958 \text{ mW}$. This power already falls below the harvestable power determined in [26]. Considering additional further power reduction measures, such as the transition to a supply voltage of 1.8 V and the implementation of more energy-efficient temperature sensors, the average power will be further reduced significantly. Thus, the results indicate that operating the measurement system using the power generated by the TEG is feasible and also buffering excess energy becomes a viable prospect.

This, however, remains the main challenge, as the power consumption of the ESP32-C3 is at least an order of magnitude higher than the power consumption of the residual sensor system depending on the operational mode. With the ESP32-C3 using Wi-Fi, for example, the time required to connect to a Wi-Fi network and then send an HTTP request is 2.18 s on average. According to [37] the ESP32-C3 consumes 276 mA during wireless transmission. Consequently, an approximation of the energy necessary for this scenario is $E_{\text{Wi-Fi}} = 276 \text{ mA} \cdot 3.3 \text{ V} \cdot 2.18 \text{ s} = 1985.544 \text{ mWs}$. This value significantly exceeds the power that can be harvested in the given period. However, the current prototype includes a gold capacitor with a capacity of 470 mF [38], enabling to save $E_{\text{cap}} = 470 \text{ mF} \cdot (5.5 \text{ V})^2 = 14217.5 \text{ mWs}$. If needed, even a gold capacitor of same construction size is available with up to 1.5 F. Thus, even when considering possible losses due to the DC-DC converter and a minimal voltage needed to operate it, the amount of energy is sufficient to power the ESP32-C3 for the given period.

4 Software realization

Optimization possibilities with regard to energy consumption are not only available on the hardware side. On the software side, for example, shorter active phases and interlacing when reading out the temperature sensors can also contribute here. It is also necessary to consider which calculations must be performed on the microcontroller and which externally. Hence, the software architecture is described, and the named aspects will be addressed.

The software implementation of the measurement system is divided into two main parts. One part comprises the software of the components inside the bearing and the other part covers the software of the corresponding remote counterpart outside the bearing. The realization details of these two parts are addressed in the following.

4.1 Intra-Bearing component software flow

Inside the bearing, there are two central sub-components. The NHS3152 implements the essential operating sequence including querying the measurement results, performing preprocessing steps and saving measurement data to be able to compute the oil gap height. The ESP32-C3 is used for the wireless communication with the data receiver. For information exchange between the NHS3152 and the ESP32-C3 an I2C connection is used.

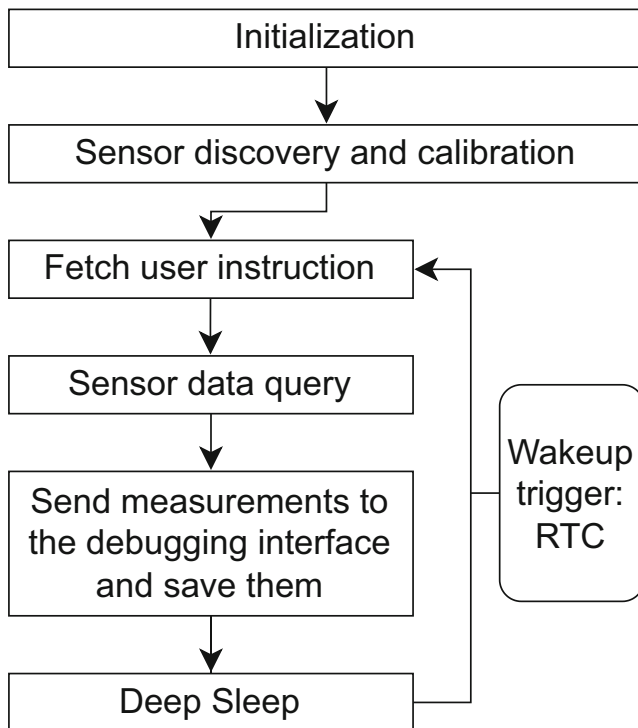


Fig. 8 Intra-bearing program flow

4.1.1 NHS3152

The microcontroller NHS3152 was programmed using the MCUXpresso IDE v11.7.1. The program flow, outlined in Fig. 8, is described followingly.

Initially the NHS3152 and all its peripherals are initialized. Subsequently a sensor discovery procedure is initiated to query how many sensors are connected and determine their specific I2C addresses. Following this, multiple temperature measurements are conducted to compute an average temperature value for calibrating each sensor. Finally, the temperature sensors are placed into sleep mode. Potential user commands like adjusting the sleep interval, precision or restarting the system are then fetched from the ESP32-C3. Additionally, initialization data including sensor information and calibration data is sent to the ESP32-C3. It's worth noting that these user commands and supplementary communication with the ESP32-C3 serves debugging purposes and raises valuable insights and information. Nevertheless, in-the-field the ESP32-C3 is intended to run only to issue an alarm when the oil gap height is undershot and if possible, when demanded e.g., by a mobile device, to retrieve status information of the sensor system. After the communication with the ESP32-C3 the main query for sensor data is started to obtain the temperature values from all sensors and the temperature data is processed. Subsequently, the measured temperatures are transmitted to the data receiver outside the bearing. Whenever the data cannot

be sent to the data receiver the data is also buffered internally to the SRAM of the NHS3152 inside a ring buffer. At present, the system can store up to 6720 temperature values within the SRAM, equating to 280 measurement points, with each point consisting of twelve temperature values. Nevertheless, this can be drastically increased if data compression is implemented [39]. Since, depending on the application, data points from several days may be necessary, an external I2C-EEPROM is intended for the next version of the prototype to be able to save significantly more measurements. The preserved data is processed in alignment with edge computing principles to ascertain the oil gap height. This approach minimizes communication overhead, thereby adhering to the conventions of a prevalent data processing methodology within the domain of the Internet of Things [40]. Nevertheless, when incorporating interpolation into the processing pipeline, a thorough evaluation is required to determine whether it should be conducted internally. Finally, the NHS3152 is put into deep sleep mode. The NHS3152 wakes up from Deep-Sleep mode after a certain amount of time using the real-time clock and restarts the temperature query process. In addition, the microcontroller can be woken up by the temperature sensors via interrupt if a certain threshold is exceeded [34, 40]. However, the energy saving depends on whether the temperature course is stationary most of the time. For this reason, such an implementation would have to be application-specific.

4.1.2 ESP32-C3

The ESP32-C3 was programmed using Visual Studio Code v1.83.1 and the PlatformIO IDE extension v3.3.1.

When powered, the ESP32-C3 starts hosting its own Wi-Fi network and a web server as a debug interface providing all necessary information on the status of the sensor system as well as all temperature values. Subsequently, the ESP32-C3 waits for incoming requests and sent data using I2C. Whenever the NHS3152 requests information the ESP32-C3 will send an answer depending on the user's last input and requests, which are done using one of the provided counterparts as described in section 4.2. Furthermore, data sent by the NHS3152 is additionally saved into the SRAM of the NHS3152 such that a longer history of temperature values can be accessed by the user. The self-hosted network can be substituted by an existing Wi-Fi network using a command sent to the ESP32-C3 via the remote counterpart.

Additionally, the hosted web server serves as an interface for Over-the-Air (OTA) updates, essential for enhancing software functionality and security. OTA updates enable seamless integration of new features and critical security patches, all facilitated without physical interventions. This OTA update functionality has already been implemented for

Fig. 9 Dashboard of the Android application for monitoring the plain bearing. (1 Control panel to change temperature precision, edit the deep sleep duration of the microcontroller, flash the NHS3152 wirelessly, restart the sensor system or switch between the hosted WiFi network and an existing WiFi network, 2 Status overview of the components, 3 Temperature overview of all sensors, 4 Temperature course of the selected sensor, 5 Different view on the data of 3 [view can be alternated by clicking the button in the upper right corner])



the ESP32-C3 and is intended to be implemented for the NHS3152 using the I2C connection to the ESP32-C3. The OTA updates can be performed by the Android application depicted in section 4.2.

4.2 Remote data receiver

The remote counterpart builds upon the web server interface provided by the ESP32-C3. Using this an Android application was implemented to monitor the sensor system in depth and to send instructions to the sensor system. An overview of the Android application and its functionalities can be seen in Fig. 9. Additionally, to simply log and monitor the temperature measurements a Python script was implemented.

5 Conclusion

In conclusion, this study has elucidated critical insights into the energy consumption dynamics of the sensor-integrating plain bearing system. The integration of advanced temperature sensors, coupled with meticulous adjustments in operational parameters such as supply voltage and clock frequency, demonstrates a promising measure for optimizing energy efficiency. The utilization of the thermoelectric generator (TEG) as a power source for the system, along

with the usage of the gold capacitor as an energy buffer for wireless communication, presents a viable prospect.

Furthermore, the strategic reduction of the sensor count, supported by temperature interpolation techniques, offers a pragmatic approach to mitigating energy consumption without compromising the system's overall efficacy. The potential benefits of these methodologies have been exemplified through preliminary experiments and will be validated using multiple approaches including inductive eddy current sensors, determining the oil gap height as a validation metric. The operating conditions of the bearing tested in chapter 2 were all in the high-speed range ($So < 1$). Higher loads and structural deformations of radial plain bearings occur in a large number of applications. These load cases will be considered further in future investigations and the limits of the applicability of temperature-based gap height determination will be examined. In future coupled TEHD-FE simulations, the influence of the measuring position on the recorded temperature and the degree to which these measured temperatures deviate from the temperatures in the lubrication gap will be investigated.

Moreover, the software architecture of the sensor system has been discussed and specific energy-saving measures were described. Further application-specific possibilities to save energy have been proposed. Finally, the debugging system using a Wi-Fi interface and an android application was outlined.

Acknowledgement Funded by the Deutsche Forschungsgemeinschaft (DFG, German Research Foundation)—441853410, 466775494

Funding Open Access funding enabled and organized by Projekt DEAL.

Conflict of interest J. Paeßens, K.-H. Kratz, T. Gemmeke, K. Kauth, T. Baszenski, B. Lehmann and G. Jacobs declare that they have no competing interests.

Open Access This article is licensed under a Creative Commons Attribution 4.0 International License, which permits use, sharing, adaptation, distribution and reproduction in any medium or format, as long as you give appropriate credit to the original author(s) and the source, provide a link to the Creative Commons licence, and indicate if changes were made. The images or other third party material in this article are included in the article's Creative Commons licence, unless indicated otherwise in a credit line to the material. If material is not included in the article's Creative Commons licence and your intended use is not permitted by statutory regulation or exceeds the permitted use, you will need to obtain permission directly from the copyright holder. To view a copy of this licence, visit <http://creativecommons.org/licenses/by/4.0/>.

References

- Tavner P, Ran L, Penman J, Sedding H (2008) Condition Monitoring of Rotating Electrical Machines
- Zhou W, Habetler TG, Harley RG (2007) Bearing Condition Monitoring Methods for Electric Machines: A General Review. IEEE, International Symposium on Diagnostics for Electric Machines, Power Electronics and Drives
- Jacobs G, Brecher C, Doncker RW, Hameyer K, Monti A, Schröder W (2017) Conference for Wind Power Drives 2017. Tagungsband Zur Konferenz
- Poll G, Deters L (2018) Lagerungen, Gleitlager, Wälzlager. Konstruktionselemente des Maschinenbaus, vol 2. Grundlagen von Maschinenelementen für Antriebsaufgaben
- M. Javaid, A. Haleem, R. P. Singh, S. Rab, R. Suman: Significance of Sensors for Industry 4.0: Roles, Capabilities, and Applications. 2. Sensors International, 2021
- Group SMA (2015) N. I. of I. Engineering (NITIE), V. Lake, Mumbai, I. R. A. Group, N. I. of I. Engineering (NITIE), V. Lake, Mumbai, I. T. A. Group, N. I. of I. Engineering (NITIE), V. Lake, Mumbai, India: Internet of Things (IoT): A Literature Review. 03. Journal of Computer and Communications
- Deckers J (2001) Entwicklung Einer Low-Cost-Körperschallsensorik Zur Überwachung Des Verschleißverhaltens von Wälz- Und Gleitgelagerten Kreiselpumpen Kleiner Leistung
- Lang OR, Steinhilper W (2013) Gleitlager: Berechnung und Konstruktion von Gleitlagern mit konstanter und zeitlich veränderlicher Belastung
- Deutsches Institut für Normung e. V.: Gleitlager – Hydrodynamische Radial-Gleitlager im stationären Betrieb: Teil 1: Berechnung von Kreiszyllinderlagern. din-de, 2017
- Deutsches Institut für Normung e. V.: Gleitlager – Hydrodynamische Radial-Gleitlager im stationären Betrieb: Teil 2: Funktionen für die Berechnung von Kreiszyllinderlagern. din-de, 2017
- Deutsches Institut für Normung e. V.: Gleitlager – Hydrodynamische Radial-Gleitlager im stationären Betrieb: Teil 3: Betriebsrichtwerte für die Berechnung von Kreiszyllinderlagern. din-de, 2017
- X. Gou, H. Xiao, S. Yang: Modeling, Experimental Study and Optimization on Low-Temperature Waste Heat Thermoelectric Generator System. 87. Applied Energy, 2010
- X. Niu, J. Yu, S. Wang: Experimental Study on Low-Temperature Waste Heat Thermoelectric Generator. 188. Journal of Power Sources, 2009
- Yildiz F, Coogler K (2014) Low Power Energy Harvesting with a Thermoelectric Generator through an Air Conditioning Condenser. 34. ASEE Annual Conference and Exposition. Conference Proceedings
- Kirchner E et al (2024) A Review on Sensor-Integrating Machine Elements. Advanced Sensor Research
- Dunham MT, Barako MT, LeBlanc S, Asheghi M, Chen B, Goodson KE (2015) Power Density Optimization for Micro Thermoelectric Generators, vol 93. Energy
- Abdal-Kadhim A, Kok SL (2017) Application of Thermal Energy Harvesting from Low-Level Heat Sources in Powering up WSN Node
- Attivissimo F, Lanzolla AML, Passaghe D, Paul M, Gregory D, Knox A (2014) Photovoltaic-Thermoelectric Modules: A Feasibility Study
- Bhattacharya M, Ranjan M, Kumar N, Maiti T (2021) Analysis and Optimization of a SnSe-Based Thermoelectric Generator, vol 4. Performance, ACS Applied Energy Materials
- Bobean C, Pavel V (2013) The Study and Modeling of a Thermoelectric Generator Module
- Bilbao A, Hoover D, Rice J, Chapman J (2011) Ultra-Low Power Wireless Sensing for Long-Term. Struct Health Monit 7981:
- Kirchner E, Martin G, Vogel S (2018) Sensor Integrating Machine Elements—Key to In-Situ Measurements in Mechanical Engineering
- Hausmann M, Kirchner E, Vorwerk-Handing G, Welzbacher P (2022) Methods for In Situ Sensor Integration. Design Methodology for Future Products: Data Driven, Agile and Flexible
- Aufischer R, Schallmeiner S, Wimmer A, Engelmayer M (2019) Intelligente Gleitlager zur Unterstützung der Motorenentwicklung, vol 80. MTZ – Motortechnische Zeitschrift
- Reynolds O (1997) IV. On the Theory of Lubrication and Its Application to Mr. Beauchamp Tower's Experiments, Including an Experimental Determination of the Viscosity of Olive Oil, vol 177. Philosophical Transactions of the Royal Society of London
- T. Baszenski, K. Kauth, K.-H. Kratz, F. Gutiérrez Guzmán, G. Jacobs, T. Gemmeke: Sensor Integrating Plain Bearings: Design of an Energy-Autonomous, Temperature-Based Condition Monitoring System. 87. Forschung im Ingenieurwesen, 2023
- J. Marheineke, G. Jacobs, K. Kauth, K.-H. Kratz, F. G. A. Gutierrez Guzman, T. Baszenski, T. Gemmeke: Auto-informative Gleitlager – Konzept einer autarken, temperaturbasierten Zustandüberwachung. 2022
- Hebenstreit H, Beilicke R (2018) Gleitlagerverschleißgrenzen II – Einsatzgrenzen von Hydrodynamischen Radialgleitlagern Infolge von Verschleiß, FVA-Abschlussbericht. FVA, pp 755–II
- Deutsches Kupferinstitut Berufsverband e. V.: Werkstoffdatenblatt: CuSn12Ni2-C. 2005
- (2022) Texas Instruments: PCA9546A Low Voltage 4-Channel I2C and SMBus Switch with Reset. Function
- NXP: NHS31xx Power Modes, NHS3152 SDK – V12.6. 2023
- NXP: UM10876, NHS3152 SDK – V12.6. 2023
- NXP: NHS31xx Data Storage, NHS3152 SDK – V12.6. 2023
- Texas Instruments: LM73 2.7-V, SOT-23, 11- to 14-Bit Digital Temperature Sensor With 2-Wire Interface. 2015
- (2018) Texas Instruments: TMP117 High-Accuracy, Low-Power, Digital Temperature Sensor With SMBus™- and I2C-Compatible Interface
- Thomas D, Wilkie E, Irvine J (2016) Comparison of Power Consumption of WiFi Inbuilt Internet of Things Device with Bluetooth Low Energy 10:
- (2023) Espressif Systems: ESP32-C3 Series Datasheet
- (2023) Eaton: KR Supercapacitors—Coin Cells. Tech Data 4327:

39. J. G. Kolo, S. A. Shanmugam, D. W. G. Lim, L.-M. Ang: Fast and Efficient Lossless Adaptive Compression Scheme for Wireless Sensor Networks. 41. Computers & Electrical Engineering, 2015
40. Krishnamurthi R, Kumar A, Gopinathan D, Nayyar A, Qureshi B (2020) An Overview of IoT Sensor Data Processing, Fusion, and Analysis. Techniques, vol 20. Sensors

Publisher's Note Springer Nature remains neutral with regard to jurisdictional claims in published maps and institutional affiliations.